OXIDE ELECTRONICS

Spatiotemporal characterization of the field-induced insulator-to-metal transition

Javier del Valle[1,2]*, Nicolas M. Vargas[1], Rodolfo Rocco[3], Pavel Salev[1], Yoav Kalcheim[1,4], Pavel N. Lapa[1], Coline Adda[1], Min-Han Lee[1,5], Paul Y. Wang[1], Lorenzo Fratino[3], Marcelo J. Rozenberg[3], Ivan K. Schuller[1]

Many correlated systems feature an insulator-to-metal transition that can be triggered by an electric field. Although it is known that metallization takes place through filament formation, the details of how this process initiates and evolves remain elusive. We use in-operando optical reflectivity to capture the growth dynamics of the metallic phase with space and time resolution. We demonstrate that filament formation is triggered by nucleation at hotspots, with a subsequent expansion over several decades in time. By comparing three case studies (VO_2, V_3O_5, and V_2O_3), we identify the resistivity change across the transition as the crucial parameter governing this process. Our results provide a spatiotemporal characterization of volatile resistive switching in Mott insulators, which is important for emerging technologies, such as optoelectronics and neuromorphic computing.

Correlated materials display a wide variety of electronic orders and phase transitions (*1*). Particularly interesting are Mott insulators, many of which show an insulator-to-metal transition (IMT) driven by electronic correlations (*2*, *3*). This transition can be induced when temperature, pressure, or doping are varied (*2*, *4*–*6*), but for some materials, it can also be triggered by the application of an electric field (*7*–*13*). The field-driven IMT results in volatile resistive switching, which makes it very promising for upcoming technologies such as optoelectronics (*14*–*16*) and neuromorphic computing (*13*, *17*–*21*). Most research has focused on transport properties, particularly on how to exploit this phenomenology for potential applications (*13*, *17*–*22*). However, many questions regarding the basic physics of the field-driven transition are still unanswered. One of them concerns the transition dynamics—the path the system takes to go from insulator to metal. Although there have been several pump-probe studies on the dynamics of the light-driven IMT (*23*–*26*), the physics of the voltage-driven transition may be quite different and involves an interplay of Joule heating, electric field lines, and temperature gradients. Unraveling the voltage-driven transition is crucial both for the basic understanding of the process and for the proper design of technological applications, but it is challenging from an experimental perspective as it requires in-operando characterization of nano- or microdevices. Several techniques have been used to successfully visualize the static (stationary) picture: Above a certain threshold voltage, metallic domains appear and arrange in a filament connecting the electrodes, with characteristic widths in the micrometer range (*27*–*29*). However, a complete picture of the field-driven IMT requires time dependence to be added to spatial resolution.

To capture the filament-formation dynamics, a probe sensitive to the metal-insulator phase fraction and capable of fast signal acquisition is needed. Techniques based on nanofocused x-rays or on conductive atomic force microscopy (c-AFM) are not well suited for time-resolved measurements. Optical reflectivity, on the other hand, has been shown to provide a very good estimate of the metallic phase fraction (*6*), and its time dependence can be easily monitored. Figure 1A shows reflectivity r as a function of temperature T, in a VO_2 thin film. A clear contrast between the reflectivity of the low-temperature insulator (r_{Ins}) and the high-temperature metal (r_{Met}) can be seen, together with the intrinsic hysteresis of the first-order phase transition. We define the normalized reflectivity $r_{norm} = (r - r_{Ins}) / (r_{Met} - r_{Ins})$ and use it as an estimate of the metallic phase fraction. We use this technique to study the transition dynamics in three well-known oxides featuring an IMT: VO_2 ($T_{IMT} \approx 340$ K), V_2O_3 ($T_{IMT} \approx 160$ K), and V_3O_5 ($T_{IMT} \approx 420$ K) (*2*, *30*). These materials have very different transition temperatures and magnitudes of the resistance change [fig. S1 (*31*)]. In V_2O_3 and VO_2, the IMT is a first-order transition accompanied by an abrupt change of the crystal lattice symmetry and dimensions (*2*, *6*). In V_3O_5, the IMT is a second-order transition and happens without a substantial structural change (*30*). This distinction allows us to examine the importance of various factors and single out the most relevant properties governing the field-driven IMT.

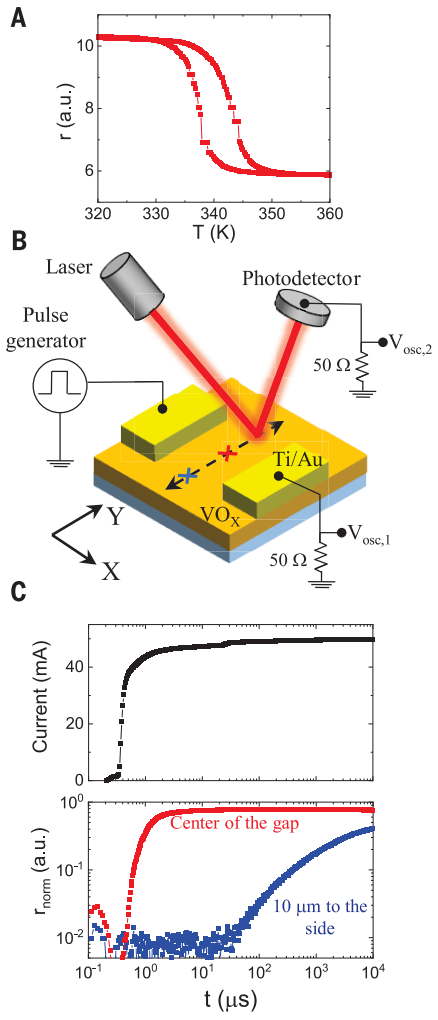

Fig. 1. Measurement of the metallic phase fraction. (**A**) Reflectivity r versus temperature T in a 100-nm-thick VO_2 film. a.u., arbitrary units. (**B**) Schematic representation of the measurement setup. Two Ti/Au electrodes (yellow) are patterned on top of a vanadium oxide film (orange), leaving a 20-μm oxide gap in between them. The IMT is induced by applying a voltage step using a function generator. A 660-nm laser is focused to a 3-μm spot between the electrodes, and the reflectivity is measured with a photodetector. Current and reflectivity are monitored with an oscilloscope. Spatial resolution is enabled by moving the laser spot in the direction perpendicular to the current. (**C**) Current (top) and reflectivity (bottom) in a VO_2 device as a function of time, when a 24-V step is applied at $t = 0$. Time axis is on a logarithmic scale. T = 333 K. The two curves in the bottom panel illustrate the different reflectivity response in two locations: the middle of the gap [red curve, position marked with a red cross in (B)] and 10 μm away from the center [blue curve, position marked with a blue cross in (B)].

Figure 1B shows a schematic representation of our experimental setup. The VO_2 and V_2O_3 films were grown using magnetron sputtering from a V_2O_3 target. In the VO_2 case, a small

[1]Department of Physics and Center for Advanced Nanoscience, University of California San Diego, La Jolla, CA 92093, USA. [2]Department of Quantum Matter Physics, University of Geneva, 1211 Geneva, Switzerland. [3]Université Paris-Saclay, CNRS Laboratoire de Physique des Solides, 91405, Orsay, France. [4]Department of Material Science and Engineering, Technion - Israel Institute of Technology, Haifa 32000, Israel. [5]Materials Science and Engineering Program, University of California San Diego, La Jolla, CA 92093, USA.
*Corresponding author. Email: javier.delvalle@unige.ch

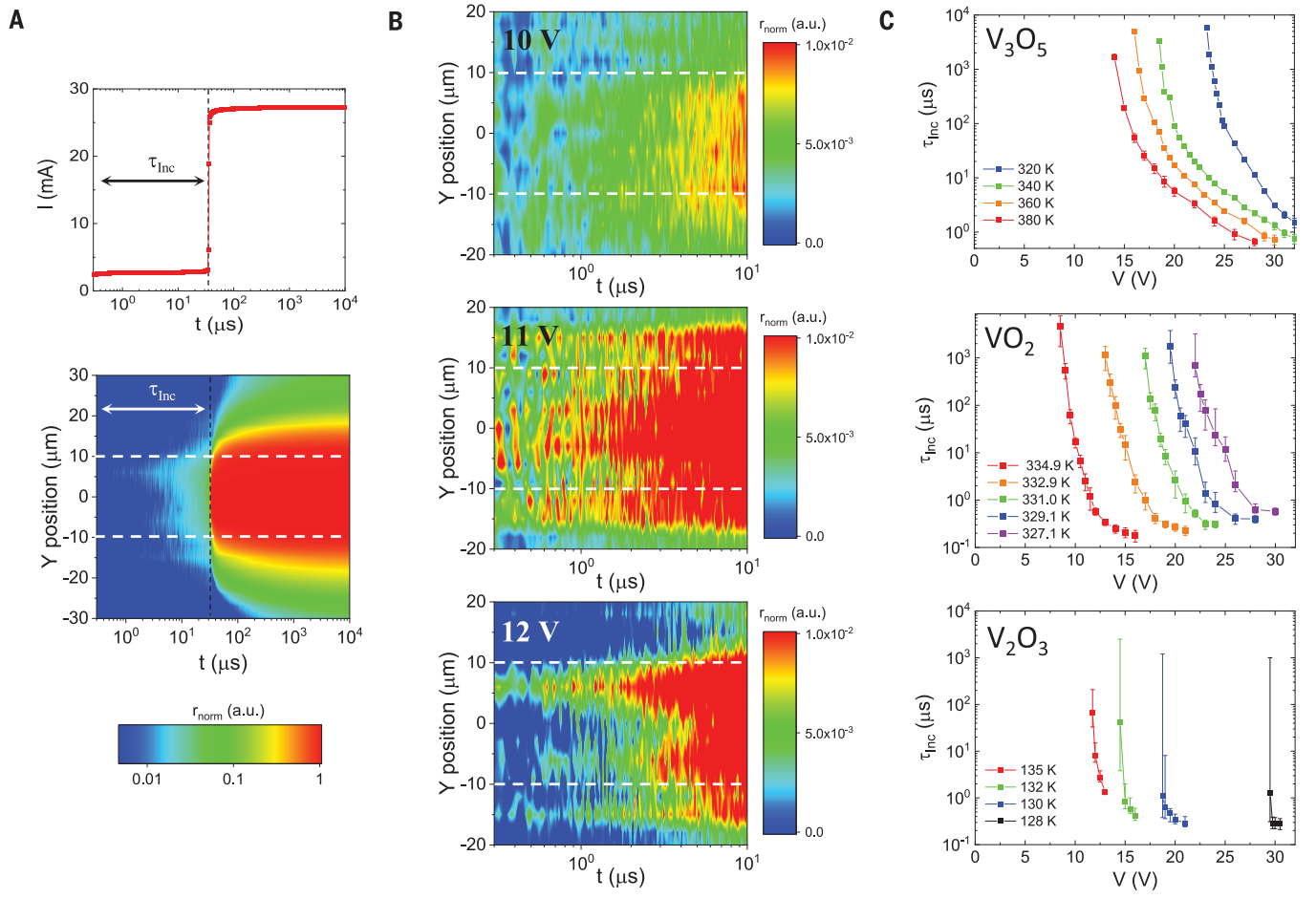

Fig. 2. Nucleation dynamics of the field-driven IMT. (**A**) (Top) Current versus time in a VO_2 device when the field-driven IMT is triggered by a 12-V step applied at t = 0. Base temperature is T = 335 K. The vertical dashed line shows the moment in which the filament percolates. (Bottom) Space- and time-resolved reflectivity, recorded at the same time as in the top panel. The reflectivity is shown on a logarithmic color scale. The horizontal axis is time in logarithmic scale, and the vertical axis corresponds to the coordinate along which the spot was scanned. The scanning direction is perpendicular to the current direction. Dashed white lines indicate the electrode width. The emergence of a filament close to 30 μs is readily visible. (**B**) Zoomed-in reflectivity maps for VO_2, for three different applied voltages: 10 V, 11 V, and 12 V. The time scale has been zoomed into the first 10 μs, and the color scale has been amplified to better appreciate the formation of hotspots before the appearance of the filament. T = 335 K. Full-scale data are shown in fig. S3 (*31*). (**C**) Incubation time (τ_{Inc}) as a function of the applied voltage, at different temperatures. The three panels correspond to the three oxides studied here: V_3O_5, VO_2, and V_2O_3.

amount of O_2 gas was added during growth to achieve the desired stoichiometry. The V_3O_5 was derived from a V_2O_3 film after an annealing in a controlled oxygen atmosphere. More details on sample fabrication and properties can be found in the supplementary materials (*31*). Metallic electrodes were patterned to define planar VO_x bridges in which resistive switching can be induced while simultaneously measuring the reflectivity. Figure S5 shows the quasistatic voltage-current characteristics of the devices. Resistive switching is completely volatile, ruling out any electroforming caused by ion migration. The electrodes are 20 μm wide with a 20-μm separation, leaving an exposed oxide gap in between. A 660-nm laser is focused to a 3-μm spot and aimed into the gap, and the reflectivity is measured using a photodetector with a time resolution of ~50 ns after signal amplification. A voltage pulse is applied across the electrodes using a function generator. The generator's output impedance is 450 ohms, which is considerably larger than the typical metallic state resistance of the devices (~10 ohms) but much lower than the insulating state resistance (>10 kilohms). Hence, our experiment can be considered voltage controlled before filament formation, and it becomes current limited afterward—a necessary condition to avoid damage. We use an oscilloscope to simultaneously record reflectivity and current. To increase signal-to-noise ratio, averaging over 100 cycles is performed for each reflectivity measurement. The voltage pulse width is a few milliseconds to characterize the device's response over several decades in time, and the separation between cycles is kept at 1 s to allow for complete cooling down and relaxation to the initial insulating state (*11*). The top panel in Fig. 1C shows the current versus time when a 24-V step is applied at time t = 0. After an incubation time of ~300 ns, a filament is formed, and the current quickly increases. The bottom panel shows the normalized reflectivity in the center of the gap (red) and 10 μm away (blue). The time axis is on a logarithmic scale. Comparing the curves, we can conclude that metallization happens fast in the center on a time scale of ~10^{-7} s and then expands at a much slower rate to the final (stationary) filament configuration.

This example illustrates how this setup offers a distinct opportunity to observe the resistive switching dynamics, allowing us to form a complete picture of the process. By repeating this measurement every 3 μm, it is possible to capture, with space and time resolution, the dynamical evolution of the field-driven IMT. This can be seen in Fig. 2A. The color scale indicates the metallic fraction, the

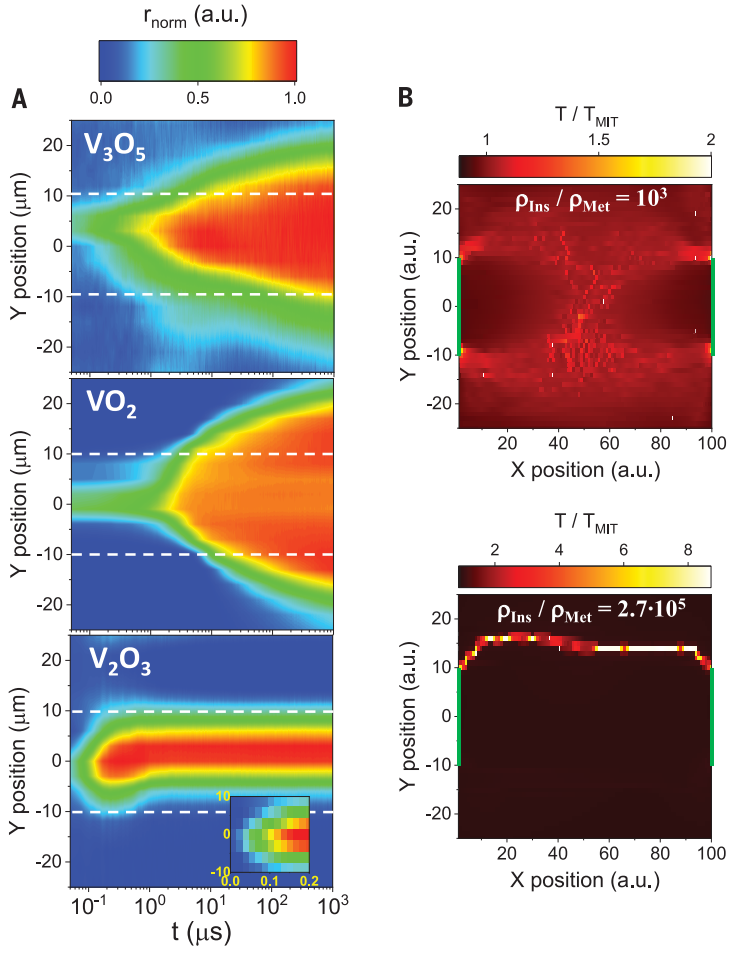

Fig. 3. Dynamics of filament expansion and role of the resistance ratio ρ_{Ins}/ρ_{Met}. (**A**) Space- and time-resolved reflectivity during the field-driven IMT. The reflectivity is coded in color scale. The horizontal axis is time on a logarithmic scale, and the *y* axis corresponds to the coordinate along which the spot was scanned, which is perpendicular to the current direction. Dashed white lines indicate the electrode width. Time is set to zero when the filament percolates, in contrast to Fig. 2, in which it was set to zero when the voltage was applied. The three panels correspond to the three materials used in this work. The measurement conditions were: V = 30 V and T = 328 K for V_3O_5; V = 20 V and T = 330 K for VO_2; and V = 32 V and T = 134 K for V_2O_3. The inset in the bottom panel shows a zoomed-in picture of the first moments of filament expansion in V_2O_3, and the time axis is in linear scale. (**B**) Simulated 2D temperature maps just after filament percolation. The *x* axis is parallel to the current direction, and the green bars mark the position of the electrodes. Base temperature in the simulation was 0.88 T_{IMT}, where T_{IMT} is the transition temperature. The top panel corresponds to a resistivity ratio $\rho_{ins}/\rho_{met} = 10^3$, and the bottom panel corresponds to $\rho_{ins}/\rho_{met} = 2.7 \times 10^5$. Because no defects are present in the simulation, the filaments originate at the electrode corners, where the electric field is the largest.

horizontal axis is the time on a logarithmic scale, and the vertical axis is a scan across the direction perpendicular to the current-filament direction. This can be interpreted as a picture of the filament width as a function of time. The dashed white lines mark the width of the electrodes. The current versus time is plotted in the top panel for comparison. There is an ~30-μs incubation time (τ_{inc}) between the initial voltage application and the filament formation, clearly identified as a sudden jump in the reflectivity map. τ_{inc} is larger than that shown in Fig. 1C because we are applying 12 V instead of 24 V (*32*). This localized reflectivity jump caused by the emergence of a metallic filament is observed for the three oxides we studied. Notably, subtle changes in r_{norm} can be observed long before the filament is formed, which points either to a partial metallization of the system or to a temperature increase within the insulating state. These changes are distributed nonuniformly, indicating the presence of nucleation points that slowly grow in size and eventually trigger the formation of a filament.

These results suggest the following qualitative scenario. As the electric field is applied, the current flows inhomogeneously, concentrated in intrinsic defects or inhomogeneities of the film. Defects tend to partially suppress the IMT and lower the film resistivity (*33*, *34*), which helps in focusing the current. As Joule heating concentrates in these hotpots, the temperature increases locally, further metallizing them and concentrating the current even more. A positive feedback loop is established, leading to an instability and ultimately filament formation. For a simple, single-element system, the thermal dynamics will follow

$$\partial T/\partial t \propto E^2/\rho(T) - \kappa \cdot (T - T_0) \quad (1)$$

where E is the electric field, $\rho(T)$ is the resistivity, T_0 is the substrate temperature, and κ is the thermal coupling constant between the film and the substrate. Equation 1 highlights the applied voltage and the temperature dependence of the resistivity as the key factors controlling the feedback loop, and changes in any of these parameters are expected to greatly affect the nucleation dynamics. This can be seen experimentally in Fig. 2B, which shows an amplified picture of the nucleation process (before percolation of the filament) for three slightly different applied voltages: 10 V, 11 V, and 12 V. The color scale has been rescaled to better visualize the small reflectivity changes associated with prefilament dynamics [full scale plots shown in fig. S3 (*31*)]. Comparing the top and bottom panels, it can be observed that even small voltage variations can result in big differences in the nucleation process. Higher voltages enhance inhomogeneous metallization, focusing the current into smaller hotspots. This accelerates the nucleation dynamics, markedly reducing the incubation time (τ_{inc}). Figure 2C shows τ_{inc} as a function of the applied voltage V, for three oxides: V_3O_5, VO_2, and V_2O_3. In all cases, subtle voltage variations can change τ_{inc} by several orders of magnitude. However, there are very noticeable differences between the three systems. The τ_{inc} sensitivity to voltage changes is relatively low for V_3O_5, higher for VO_2, and very high for V_2O_3. In the V_2O_3 case, it approaches an all-or-nothing behavior, with τ_{inc} decreasing from infinity to a few microseconds with a <1% increase in voltage.

These differences between materials are observed not only during nucleation but also after filament percolation. Figure 3A shows again the metallic fraction as a function of time and Y position. Whereas in Fig. 2 t = 0 is set when the voltage is applied, here we assigned t = 0 to the moment when the filament percolates, which can be identified by an abrupt current jump. This allows us to disregard nucleation dynamics and observe—on logarithmic time scale—a different process: filament expansion. The three oxides are shown, and whereas VO_2 and V_3O_5 seem to behave qualitatively in a similar way, V_2O_3 does not. For V_3O_5 and VO_2, the filament is initially confined to a narrow path, but it immediately starts widening and eventually reaches its final shape. Notably, this growth does not happen at a constant rate but spans multiple decades in time—i.e., there is no characteristic time scale. The expansion over the first microsecond is comparable to the growth over the following 10 μs, which is in turn similar to the subsequent

100 μs. After 0.1 to 1 ms, the filament starts converging to a stationary configuration. This behavior can be understood in terms of current fanning. As the filament grows thicker, the current density goes down, causing a decrease in Joule heating and local temperature. As a result, heat flowing from the filament into the neighboring areas becomes smaller, reducing growth rate. At first glance, the growth dynamics of V_2O_3 look completely different when compared with VO_2 and V_3O_5. The filament reaches a stationary configuration in 1 to 2 μs, remaining unaltered after that. The inset in the bottom panel of Fig. 3A shows a zoomed-in picture of the first 600 ns. Filament expansion is actually clearly visible but at a much higher speed: Whereas the initial growth rate is ~0.3 m/s for V_3O_5 and 1 to 2 m/s for VO_2, in V_2O_3 it is on the order of 100 m/s.

This trend—V_3O_5 having the slowest dynamics and V_2O_3 the fastest—is present both in filament nucleation (Fig. 2C) and in filament expansion (Fig. 3A). To understand this, it is important to consider the other key factor controlling the metallization feedback loop—the temperature dependence of the resistivity (Eq. 1). This dependence is steeper the larger the magnitude of the IMT, which is given by the resistivity ratios (ρ_{ins}/ρ_{met}) between the insulating and metallic states. ρ_{ins}/ρ_{met} actually varies a lot between the three oxides studied here, being ~10 for V_3O_5, ~10^3 for VO_2, and >10^5 for V_2O_3 (fig. S1).

To investigate how ρ_{ins}/ρ_{met} affects the nucleation and growth dynamics, we modeled our device as a resistor network [see further discussion and fig. S9 in (*31*)]. Each node in the network can be either insulating or metallic, depending on the local temperature through a Landau-type free energy functional that mimics a first-order phase transition (*11*, *35*), similar to the IMT present in VO_2 and V_2O_3. This functional depends only on the temperature, without any direct contribution from the electric field. This implies that in our simulations, the IMT can only be triggered either by Joule heating or by increasing the overall temperature. At each simulation step, temperature, voltage, and current distributions are updated, providing information about the system dynamics. Figure 3B shows two-dimensional (2D) temperature maps just after the filament percolates for two different cases: $\rho_{ins}/\rho_{met} = 10^3$ and $\rho_{ins}/\rho_{met} = 2.7 \times 10^5$. Because intrinsic defects are not included in the simulations, the filaments form at the corners of the electrodes, which are the points of maximum electric field. For larger ρ_{ins}/ρ_{met}, the current concentrates into a much narrower path, and the nucleation is more heterogeneous. Localized nucleation focuses Joule heating into smaller regions, amplifying the feedback loop and accelerating the nucleation dynamics. This explains why τ_{inc} is much more sensitive to small voltage increments in V_2O_3 ($\rho_{ins}/\rho_{met} \approx 10^5$) than in VO_2 ($\rho_{ins}/\rho_{met} \approx 10^3$). Once percolation takes place, the filament starts widening—a feature also captured by the simulations (fig. S10). The initial rate at which it grows is proportional to its temperature. As can be seen in Fig. 3B, the filament temperature is higher for larger ρ_{ins}/ρ_{met}, providing a qualitative explanation for the different expansion rates observed in Fig. 3A. The role of system inhomogeneity has been previously explored in (*36*), where a similar conclusion was reached, with higher ρ_{ins} leading to smaller metallic regions with the subsequent increase of local current density.

According to our simulations, for large ρ_{ins}/ρ_{met}, a very small volume of the sample controls the initial nucleation. This renders the metallization of the whole device sensitive to local fluctuations, markedly increasing stochasticity. This picture is supported by τ_{inc} error bars in Fig. 2C, which are barely visible for V_3O_5, are noticeable for VO_2, and are very large for V_2O_3, indicating that stochastic behavior in filament formation increases with an increasing ρ_{ins}/ρ_{met} ratio. As a consequence, V_2O_3 is affected by intense cycle-to-cycle variation [see further discussion and fig. S11 in (*31*)]. VO_2 and V_3O_5 do not show comparable cycle-to-cycle variations. Although our simulations do not consider defects, our samples feature some device-to-device variability, possibly owing to intrinsic disorder. Even though this leads to noticeable differences in the quasi-static voltage-current characteristics [fig. S5C (*31*)], reflectivity measurements show that filament nucleation and growth dynamics are very similar for different devices [fig. S12 (*31*)].

Although the ρ_{ins}/ρ_{met} ratio seems to account for most differences between the three oxides, we must also consider other possibilities. The three materials feature very diverse transition temperatures, which could lead to large changes in the parameters that control thermal dynamics. A larger effective thermal conductivity κ_{eff} would naturally accelerate the switching process. Our films are grown on top of sapphire, which has a large κ that increases with lowering temperature and could contribute to the differences between VO_2 and V_2O_3. However, the vanadium films are one-tenth to one-hundredth as thermally conductive as sapphire. This makes vertical conduction across the thin film, and not the substrate, the dominant term that determines heat conductance into the environment. According to finite element simulations in (*37*), in our films, temperature drops almost to the environment value before reaching the sapphire interface. Considering that the thermal conductivities for the three oxides are very similar at our measuring temperatures (0.030 W/K per centimeter at 330 K for V_3O_5, 0.045 W/K per centimeter at 330 K for VO_2, and 0.035 W/K per centimeter at 130 K for V_2O_3) (*38*), we expect our three devices to have comparable κ_{eff} values. So, although it is possible that variations in κ could enhance the differences between these oxides, we still expect ρ_{ins}/ρ_{met} to be the key parameter. This is best appreciated when comparing the switching of VO_2 and V_3O_5 at the same temperature, when the sapphire thermal conductivity is similar [fig. S13 (*31*)]—its low ρ_{ins}/ρ_{met} ratio makes insulating V_3O_5 very leaky and drastically reduces the sharpness of the transition between low- and high-current states.

Our results show that growth and percolation of the metallic phase during the field-driven IMT can be explained just by considering the effect of Joule heating. However, this does not necessarily imply that Joule heating triggers the transition of the first metallic domains. Although this is likely the case for VO_2 (*39*, *40*), recent studies in V_2O_3 have shown that the IMT can be triggered directly by the electric field (*12*, *37*), possibly by carrier injection into the conduction band and destabilization of the insulating phase (*36*, *41*). Whether Joule heating or field effect are responsible for the transition of the first metallic domains does not affect the interpretation of the results shown here. Once a small portion of the sample undergoes the IMT, the current increases and Joule heating takes over, becoming the main driving force governing the nucleation and subsequent growth of the filament. The clear filament thickening after percolation observed for all three materials is a clear hallmark of this process, and it would not be expected if the electric field drove the growth dynamics. Notably, ρ_{ins}/ρ_{met} can account on its own for the quantitative differences between V_3O_5, VO_2, and V_2O_3. Other factors, such as the presence of a coupled structural phase transition or whether the IMT is first or second order, do not seem to play a fundamental role. Our results unveil a complete picture of the field-induced IMT and identify the key parameters that control switching speed, which is vital for proper material selection and device design in emerging information technologies, such as optoelectronics and neuromorphic computing.

REFERENCES AND NOTES

1. D. N. Basov, R. D. Averitt, D. Hsieh, *Nat. Mater.* **16**, 1077–1088 (2017).
2. M. Imada, A. Fujimori, Y. Tokura, *Rev. Mod. Phys.* **70**, 1039–1263 (1998).
3. D. Lee *et al.*, *Science* **362**, 1037–1040 (2018).
4. S. Lupi *et al.*, *Nat. Commun.* **1**, 105 (2010).
5. J. H. Park *et al.*, *Nature* **500**, 431–434 (2013).
6. Y. Kalcheim *et al.*, *Phys. Rev. Lett.* **122**, 057601 (2019).
7. G. Stefanovich, A. Pergament, D. Stefanovich, *J. Phys. Condens. Matter* **12**, 8837–8845 (2000).
8. Y. Zhou *et al.*, *IEEE Electron Device Lett.* **34**, 220–222 (2013).
9. P. Stoliar *et al.*, *Adv. Mater.* **25**, 3222–3226 (2013).
10. J. S. Brockman *et al.*, *Nat. Nanotechnol.* **9**, 453–458 (2014).
11. J. Del Valle *et al.*, *Nature* **569**, 388–392 (2019).
12. Y. Kalcheim *et al.*, *Nat. Commun.* **11**, 2985 (2020).
13. S. Kumar, J. P. Strachan, R. S. Williams, *Nature* **548**, 318–321 (2017).
14. M. Liu *et al.*, *Nature* **487**, 345–348 (2012).
15. N. A. Butakov *et al.*, *ACS Photonics* **5**, 4056–4060 (2018).

16. P. Markov *et al*., *ACS Photonics* **2**, 1175–1182 (2015).
17. J. del Valle, J. G. Ramírez, M. J. Rozenberg, I. K. Schuller, *J. Appl. Phys.* **124**, 211101 (2018).
18. Y. Zhou, S. Ramanathan, *Proc. IEEE* **103**, 1289–1310 (2015).
19. M. D. Pickett, G. Medeiros-Ribeiro, R. S. Williams, *Nat. Mater.* **12**, 114–117 (2013).
20. J. Del Valle, P. Salev, Y. Kalcheim, I. K. Schuller, *Sci. Rep.* **10**, 4292 (2020).
21. W. Yi *et al*., *Nat. Commun.* **9**, 4661 (2018).
22. B.-J. Kim, Y. W. Lee, S. Choi, S. J. Yun, H.-T. Kim, *IEEE Electron Device Lett.* **31**, 14–16 (2010).
23. S. Wall *et al*., *Science* **362**, 572–576 (2018).
24. B. T. O'Callahan *et al*., *Nat. Commun.* **6**, 6849 (2015).
25. V. R. Morrison *et al*., *Science* **346**, 445–448 (2014).
26. A. Singer *et al*., *Phys. Rev. Lett.* **120**, 207601 (2018).
27. S. Guénon *et al*., *EPL* **101**, 57003 (2013).
28. H. Madan, M. Jerry, A. Pogrebnyakov, T. Mayer, S. Datta, *ACS Nano* **9**, 2009–2017 (2015).
29. S. Kumar *et al*., *Adv. Mater.* **25**, 6128–6132 (2013).
30. U. Schwingenschlögl, V. Eyert, *Ann. Phys.* **13**, 475–510 (2004).
31. Materials and methods are available as supplementary materials.
32. G. Seo *et al*., *IEEE Electron Device Lett.* **32**, 1582–1584 (2011).
33. D. Wickramaratne, N. Bernstein, I. I. Mazin, *Phys. Rev. B* **99**, 214103 (2019).
34. Z. Shao, X. Cao, H. Luo, P. Jin, *NPG Asia Mater.* **10**, 581–605 (2018).
35. F. Tesler *et al*., *Phys. Rev. Appl.* **10**, 054001 (2018).
36. H.-T. Kim *et al*., *New J. Phys.* **6**, 52 (2004).
37. I. Valmianski *et al*., *Phys. Rev. B* **98**, 195144 (2018).
38. V. N. Andreev, F. A. Chudnovskii, A. V. Petrov, E. I. Terukov, *Phys. Stat. Sol.* **48**, K153–K156 (1978).
39. A. Zimmers *et al*., *Phys. Rev. Lett.* **110**, 056601 (2013).
40. D. Li *et al*., *ACS Appl. Mater. Interfaces* **8**, 12908–12914 (2016).
41. G. Mazza, A. Amaricci, M. Capone, M. Fabrizio, *Phys. Rev. Lett.* **117**, 176401 (2016).
42. J. del Valle *et al*., Data from Spatiotemporal characterization of the field-induced insulator-to-metal transition, Zenodo (2021); http://doi.org/10.5281/zenodo.4789471.
43. fairfriend92/mrn_simulator_releases: Spatiotemporal characterization of the field-induced insulator-to-metal transition, version 1.1, Zenodo (2021); http://doi.org/10.5281/zenodo.4813152.

ACKNOWLEDGMENTS

The authors thank G. Kassabian and J. Trastoy for helpful discussions. **Funding:** This work was supported as part of the Quantum Materials for Energy Efficient Neuromorphic Computing (Q-MEEN-C) Energy Frontier Research Center (EFRC), funded by the US Department of Energy, Office of Science, Basic Energy Sciences, under award no. DE-SC0019273. Part of the fabrication process was done at the San Diego Nanotechnology Infrastructure (SDNI) of the University of California San Diego, a member of the National Nanotechnology Coordinated Infrastructure (NNCI), which is supported by the National Science Foundation under grant ECCS-1542148. J.d.V. thanks the Swiss National Science Foundation for an Ambizione Fellowship (no. PZ00P2_185848) that supported him while writing the manuscript. R.R. is supported by the project "MoMA" from the French ANR (no.19-CE30-0020). Y.K. acknowledges funding from the Norman Seiden Fellowship for Nanotechnology and Optoelectronics. **Author contributions:** J.d.V. and I.K.S. conceived the project; J.d.V., P.S., Y.K., C.A., and M.-H.L. fabricated the samples; J.d.V. and N.M.V. measured the devices with assistance from P.S. and P.N.L.; R.R., P.Y.W., L.F., and M.J.R. performed the numerical simulations. All authors participated in the discussion and interpretation of the results. J.d.V. wrote the manuscript with input and corrections from all authors. **Competing interests:** The authors declare no competing financial or nonfinancial interests. **Data and materials availability:** Experimental data (*42*) and simulation codes (*43*) are available at Zenodo, a CERN-operated public repository.

SUPPLEMENTARY MATERIALS

science.sciencemag.org/content/373/6557/907/suppl/DC1
Materials and Methods
Supplementary Text
Figs. S1 to S13
References (*44*–*48*)

20 July 2020; accepted 8 July 2021
Published online 22 July 2021
10.1126/science.abd9088

Spatiotemporal characterization of the field-induced insulator-to-metal transition

Javier del ValleNicolas M. VargasRodolfo RoccoPavel SalevYoav KalcheimPavel N. LapaColine AddaMin-Han LeePaul Y. WangLorenzo FratinoMarcelo J. RozenbergIvan K. Schuller

Science, 373 (6557), • DOI: 10.1126/science.abd9088

Watching a metal filament grow

Resistive switching is a process in which the electrical resistance of a sample changes abruptly in response to a voltage pulse, often by orders of magnitude. This process is at the heart of many neuromorphic computing approaches but visualizing it in both space and time is tricky. del Valle *et al*. monitored the resistive switching in three different vanadium oxide compounds by measuring time- and space-resolved optical reflectivity (see the Perspective by Hilgenkamp and Gao). A characteristic conducting filament was quickly nucleated on the inhomogeneities in the sample and then propagated due to Joule heating. —JS